Journal of Adhesion Science and Technology

Publication details, including instructions for authors and subscription information:
http://www.tandfonline.com/loi/tast20

Droplet Actuation by Electrowetting-on-Dielectric (EWOD): A Review

Wyatt C. Nelson [a] & Chang-Jin 'CJ' Kim [a]

[a] Mechanical and Aerospace Engineering Department, University of California, Los Angeles (UCLA), Los Angeles, CA, 90095, USA

Version of record first published: 18 May 2012

To cite this article: Wyatt C. Nelson & Chang-Jin 'CJ' Kim (2012): Droplet Actuation by Electrowetting-on-Dielectric (EWOD): A Review, Journal of Adhesion Science and Technology, 26:12-17, 1747-1771

To link to this article: http://dx.doi.org/10.1163/156856111X599562

VSP Journal of Adhesion Science and Technology 26 (2012) 1747–1771

Journal of ADHESION SCIENCE and TECHNOLOGY
brill.nl/jast

Droplet Actuation by Electrowetting-on-Dielectric (EWOD): A Review

Wyatt C. Nelson and Chang-Jin 'CJ' Kim *

Mechanical and Aerospace Engineering Department, University of California, Los Angeles (UCLA), Los Angeles, CA 90095, USA

Abstract

This paper reviews publications that have fortified our understanding of the electrowetting-on-dielectric (EWOD) actuation mechanism. Over the last decade, growing interest in EWOD has led to a wide range of scientific and technological investigations motivated by its applicability in microfluidics, especially for droplet-based optical and lab-on-a-chip systems. At this point in time, we believe that it is helpful to summarize the observations, insights, and modeling techniques that have led to the current picture showing how forces act on liquid droplets and how droplets respond in EWOD microfluidic devices. We discuss the basic physics of EWOD and explain the mechanical response of a droplet using free-body diagrams. It is our hope that this review will inspire new research approaches and help design useful devices.

Keywords

Electrowetting, electrowetting-on-dielectric, EWOD, droplet actuation, digital microfluidics

1. Motivation

The electrowetting mechanism, especially in the configuration of electrowetting-on-dielectric (EWOD) [1–4], is a versatile tool in microfluidics because it enables control over fluid shape and flow by electrical signals alone. A popular scheme called 'digital microfluidics[1]' by EWOD actuation involves creating individual droplets from a reservoir and independently manipulating (e.g., transport, division, addition) them over a planar electrode array. For their simplicity (i.e., no pumps or valves) and reconfigurability (i.e., no hardwired fluid pathways), such microfluidic chips have been implemented in a wide range of lab-on-a-chip applications, demonstrating the potential of EWOD digital microfluidics as a miniature plat-

* To whom correspondence should be addressed. E-mail: cjkim@ucla.edu

[1] In digital microfluidics, droplets of sub-millimeter size are manipulated individually, i.e., each can be controlled independently (e.g., by EWOD actuation). Digital microfluidics can be classified as a subset of droplet microfluidics, which also includes manipulation of droplets as a group; a typical example is multiple droplets moving with a carrier fluid pumped in a microchannel.

DOI:10.1163/156856111X599562

form for generalized biochemistry [5–9]. To help advance the technology further and promote research and development for an expanding range of applications, we summarize what we have learned from many researchers in recent years about the physics of EWOD and actuation of droplets by EWOD. This summary focuses on the fundamentals of how droplets move by EWOD actuation rather than device fabrication or applications of the technology.

2. Electrocapillarity to EWOD-Driven Droplet Generation

2.1. Electrocapillarity and Electrowetting

Since Gabriel Lippmann's experiments demonstrating electrocapillarity over one hundred years ago [10], the ability to change physical properties at phase boundaries using applied electric fields has been widely known. Over the last few decades, researchers have developed techniques that harness this effect for liquid actuation at small scales [11, 12] (e.g., below the capillary length $\lambda_c = \sqrt{\gamma/\rho g}$ (γ: liquid surface tension, ρ: liquid density, g: gravitational acceleration) of water, i.e., 2–3 mm), and have even explored the possibility of designing micromachines based on the effect [13, 14]. Demonstrated examples for specific applications include variable-focus liquid lenses [15], optical displays [16, 17], mirrors [18], electrical [19] and thermal [20] switches, a tensiometer [21], rheometers [22, 23] and many digital (droplet) microfluidic devices for bioanalysis [5, 7, 8]. The development of these technologies in the last decade has been spurred by the ability to construct sub-millimeter scale components using micro-electro-mechanical systems (MEMS) manufacturing methods.

Given the variety of configurations in which liquids are actuated, specific terms are available (e.g., electrowetting and electrocapillarity) to describe the fluid response. Electrowetting is used to describe the electrically induced spreading of a liquid onto a solid and observed contact angle reduction [12, 24–26]. Electrocapillarity is used to describe the electrically induced capillary action and curvature change of the meniscus between a liquid metal (e.g., mercury) and electrolyte [10, 12, 25], exemplified by Lippmann's electrometer. Note that in a capillary having a diameter D less than the capillary length scale, the meniscus curvature is expressed with the contact angle as $(2/D)\cos\theta$. These naming conventions of electrocapillarity and electrowetting, however, are not always followed in the literature. For example, electrocapillary has been used to describe electrowetting inside a capillary [27] which was apparently before the term electrowetting became common. Also, 'continuous electrowetting' involves modification of the interfacial properties between liquid metal and electrolyte inside a capillary in order to generate continuous flows [11]. Interestingly, droplet pumping by continuous electrowetting is characterized by an initial contact angle change at the advancing meniscus (indicating a pressure gradient within the droplet), followed by steady motion during which there is no observable difference in curvatures at the front and rear ends of the droplet [13].

2.2. From Electrocapillarity to the Electrowetting Equation

The electrowetting equation can be obtained through an interfacial energy-based description of electrocapillarity, which incorporates a straightforward concept: electric field-induced charge accumulation at the solid–liquid interface, e.g., by the electrical double layer (EDL), decreases the associated interfacial tension (energy). Indeed, one may observe (at actuation voltages low enough not to break down the EDL) that the electrical energy added to the system ($c_{\mathrm{H}}V^2/2$, see below for the notations) amounts to an apparent reduction in solid–liquid interfacial tension, which is inferred from measuring the contact angle and plugging it into the Young equation, while assuming that all other interfacial tensions are unchanged by voltage. To derive the electrowetting equation by the thermodynamic principle of minimization of Gibbs free energy, we begin by listing the relevant equations:

$$-\rho_{\mathrm{S}} = \left.\frac{\partial \gamma}{\partial V}\right|_{\mu} \qquad \begin{array}{l}\rho_{\mathrm{S}}\text{: interfacial charge density,}\\ \gamma\text{: interfacial tension,}\\ V\text{: voltage (across the interface),}\\ \mu\text{: chemical potential,}\end{array} \tag{1a}$$

$$c_{\mathrm{H}} = \frac{\partial \rho_{\mathrm{S}}}{\partial V} \qquad \begin{array}{l}c_{\mathrm{H}}\text{: Helmholtz capacitance per unit area}\\ \text{of solid–liquid interface,}\end{array} \tag{1b}$$

$$\gamma_{\mathrm{sl}}(V) = \gamma_{\mathrm{sl}}(0) - \frac{c_{\mathrm{H}}}{2}V^2 \qquad \begin{array}{l}V\text{: applied voltage minus potential}\\ \text{of zero charge,}\\ \gamma_{\mathrm{sl}}\text{: solid–liquid interfacial tension,}\end{array} \tag{1c}$$

$$\gamma\cos\theta = \gamma_{\mathrm{sf}} - \gamma_{\mathrm{sl}} \qquad \begin{array}{l}\text{Young equation,}\\ \gamma\text{: liquid–fluid interfacial tension,}\\ \gamma_{\mathrm{sf}}\text{: solid–fluid interfacial tension,}\end{array} \tag{1d}$$

$$\cos\theta = \cos\theta_0 + Ew \qquad \text{Electrowetting equation,} \tag{1e}$$

$$Ew = \frac{c_{\mathrm{H}}V^2}{2\gamma} \qquad \text{Electrowetting number.} \tag{1f}$$

The differential relationship between interfacial tension, voltage and interfacial charge density formulated by Lippmann (equation (1a)) is integrated, assuming a constant Helmholtz layer capacitance per unit area (equation (1b)) to obtain an equation for a voltage-dependent solid–liquid interfacial tension (equation (1c)). This equation is then combined with the Young equation (equation (1d)) in order to arrive at the electrowetting equation (equation (1e)). The dimensionless electrowetting number *Ew* (equation (1f)) expresses the importance of electrical energy at the solid–liquid interface (the amount by which the interfacial energy of the solid–

liquid interface is reduced) relative to the interfacial energy at the liquid–fluid[2] interface.

The electrowetting equation in the form of equation (1e) can be applied to a configuration of EWOD, which we will discuss in the following section, by simply replacing c_H with c_d, the capacitance of a thin-film dielectric layer, and V with $V_{applied}$, an externally applied voltage [1, 2, 28]. The implication of the former substitution is that the dielectric layer(s) is part of a pseudo-interface between the liquid and solid electrode. The implication of the latter substitution is that essentially all of the externally applied voltage drops across the above pseudo-interface, i.e., voltage drops within the liquid, e.g., EDL, are negligible. Those interested in the thermodynamic interpretations of the conventional electrowetting (i.e., electrowetting on conductor) and EWOD in more detail may consult the review by Moon and Kim [29]. Importantly, the EWOD configuration prompted the development of electromechanical modeling techniques that can provide a more direct description of the EWOD force than the thermodynamic energy minimization-based consideration (*via* the Young equation) that resulted from the original observations of electrocapillarity.

2.3. Electrowetting-on-Dielectric (EWOD)

Electrowetting-on-dielectric describes a configuration in which an insulating layer separates the working liquid and actuation electrodes [1, 2, 27, 28]. Despite the much higher voltage needed, e.g., 100's of volts in the early days [24, 27] and 15–80 V in air in present days, EWOD is the preferred arrangement over the traditional direct electrowetting on conductor (which uses a potential below 2 V) for two main reasons: (i) insulators guard working fluids from electrodes, thereby allowing a much higher electric field (i.e., stronger electrowetting effect) before an electrical leakage or breakdown (see Fig. 3 of [28]), and (ii) one can coat a thin layer of very hydrophobic material, on which the contact angle hysteresis is small and thereby working fluids move easily. Because of these attributes, a wide variety of droplet-medium combinations can be manipulated, e.g., water in air [1], water in oil [4], oil-encapsulated water in air [30, 31], oil in air [31], gas in water [32], etc. In EWOD devices, much of the applied voltage is sustained by the dielectric layer, so the electric field distribution and associated electrowetting forces are linked primarily to the thickness and physical properties of the dielectric. In preparation for the more in-depth discussions to follow, the reader may find it helpful to keep in mind the several key points about EWOD systems:

- While their surfaces in contact with a solid necessarily acquire a net charge during actuation, droplets in common EWOD devices (Fig. 2) maintain electroneutrality because they are insulated from the electrodes. EWOD droplet

[2] The liquid–fluid interface can be liquid–gas, liquid–vapor or liquid–liquid if immiscible liquids. Although a liquid–air system may be most representative, liquid–liquid systems of aqueous solution and oil are found in many electrowetting devices.

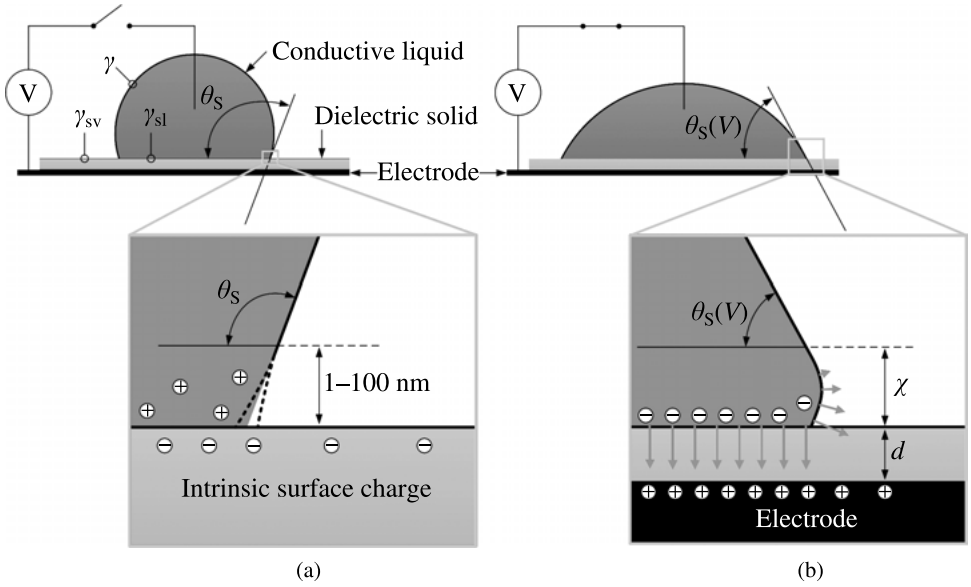

Figure 1. The static contact angle of a conductive liquid on an EWOD surface surrounded by a dielectric fluid (a) under no voltage and (b) under voltage. For the boxed drawings enlarged for the contact line region, (a) is more magnified than (b). In (b), χ is on the order of d, which is on the order of 1 μm in many EWOD devices.

actuation in this scenario is therefore analogous to particle dielectrophoresis (DEP) [33]. In contrast, in common EWOD spreading experiments with an electrode directly contacting a sessile droplet (Fig. 1), the droplet can acquire a net charge [34].

- Because EWOD droplets have finite conductivity, the electrical field formed within the liquid as a response to the applied actuation voltage is a function of actuation frequency. At low frequencies, the internal field is low, and EWOD forces are localized to the contact line. At high frequencies, the internal field is high and EWOD forces are more evenly distributed along the liquid–fluid interface. More details are provided in Section 4.2.

- Energy-based derivations of EWOD forces rarely account for edge effects, e.g., fringe capacitance. Events at the edges are central, however, to understanding the spatial distribution of EWOD forces, contact angle hysteresis and saturation, static and dynamic wetting phenomena, and failure mechanisms such as dielectric charging and breakdown.

- The minimum EWOD force required to initiate droplet actuation depends on the resistance forces preventing movement, or de-pinning, of the contact line. This resistance can be thought of as static friction and it is usually quantified in terms of contact angle hysteresis. EWOD systems use low-energy solid surfaces, e.g., Teflon® and Cytop®, primarily because they exhibit low contact

angle hysteresis with a wide range of liquids; the magnitude of the contact angle is not necessarily important with respect to the minimum EWOD actuation force. For systems with high hysteresis, e.g., water on glass in air, EWOD forces may not be sufficient to initiate droplet movement. On the other hand, contact line resistance prevents unwanted movement of droplets by external vibrations, shocks, etc., making the EWOD device stable against inertial effects.

- Limitations on the electrowetting force with respect to the contact angle and the associated field intensification at the contact line are not fully specified, but are observed to coincide with various dissipation mechanisms occurring at the contact line, e.g., leakage current, dielectric charging and satellite droplet ejection. Though important and under investigation by many, these issues are not yet well understood and not covered in this review.

2.4. EWOD Actuation Benchmarks

In 1969, Dahms [27] reported apparently the first experiments using an EWOD configuration. His interest was in the electrocapillary response, analogous to Lippmann's and not specifically in the contact angle change. In 1993, Berge [2] showed experimentally that the voltage-induced contact angle reduction observed traditionally for a droplet on a conducting surface (i.e., by electrowetting [12]) can also be observed on an insulating surface (i.e., by EWOD) covering a conductor. The main benefits of EWOD over conventional electrowetting were, thus, demonstrated, i.e., electrical force could be applied to a wide range of liquids without risking premature electrochemical breakdown, and reversibility was achieved using a low surface energy material with a low associated contact angle hysteresis, allowing the contact lines to move easily. This was a crucial development in enabling other researchers to extend the use of EWOD actuation from sessile droplet spreading to droplet translation and splitting. Since Berge [2], various EWOD configurations and platforms have been reported. Table 1 is a list of benchmark achievements in technology development towards EWOD digital microfluidics during the early proof-of-concept era. This list is not meant to be exhaustive, but rather to provide a timeline from demonstrations of EWOD liquid actuation in a capillary [27] to the core digital microfluidic operations, i.e., droplet creation, translation, addition and division [35]. Not included are theoretical work and developments beyond the core droplet operations, including applications of digital microfluidics.

3. Basic Physics of EWOD

3.1. The Static Contact Angle

The Young equation defines a static contact angle θ_S that satisfies a minimum of total interfacial energy in a solid–liquid–fluid system. It is assumed that the shape of the liquid–fluid phase boundary is influenced by interfacial energies only, and these interfacial energies are not influenced by other interfaces as a result of disjoining

Table 1.
Benchmark achievements in EWOD during the early proof-of-concept phase: from the first EWOD configuration up to core droplet operations

Year	Title	Comments	Reference
1969	Electrocapillary measurements at the interface insulator-electrolytic solution	Demonstrates EWOD in a capillary	Dahms [27]
1980	An investigation into the mechanisms of water treeing in polyethylene high-voltage cables	Demonstrates contact angle of a water droplet polyethylene as a function of applied voltage	Minnema *et al.* [36]
1990	Preliminary investigation of micropumping based on electrical control of interfacial tension	Proposes microdevices for electrowetting, continuous electrowetting and EWOD	Colgate and Matsumoto [37]
1993	Electrocapillarity and wetting of insulator films by water	Sessile droplet spreading by EWOD	Berge [2]
1996	Electrowetting of water and aqueous solutions on PET insulating films	Sessile droplet spreading by EWOD	Vallet *et al.* [24]
1998	Electrostatic actuation of liquid droplets for microreactor applications	Electrostatic transport of droplets using distant electrodes	Washizu [38]
2000	Electrowetting-based actuation of liquid droplets for microfluidic applications	Parallel-plate EWOD droplet transport in oil medium	Pollack *et al.* [4]
2002	Electrowetting and EWOD of liquid droplets for microscale liquid handling	Parallel-plate EWOD liquid manipulation in air	Lee *et al.* [1]
2002	Low voltage EWOD	Droplet translates in air with 15 V	Moon *et al.* [28]
2003	Creating, transporting, cutting, and merging liquid droplets by electrowetting-based actuation for digital microfluidic circuits	Parallel-plate EWOD droplet creation and splitting in air	Cho *et al.* [35]

pressures [39]. Also, line tension is neglected [40]. However, there is debate as to whether or not the contact angle given by the Young equation should be called the *equilibrium* contact angle, because, in most cases, non-equilibrium heat and mass transfer processes such as evaporation and surface adsorption are neglected [41]. For example, before we place a droplet on a surface in a gas, we may attribute a solid–gas energy γ_{sg} to the interface (i.e., the amount of energy required to create a unit of interfacial area). Now, consider we place a droplet that partially wets the surface (e.g., water on plastic). Since the liquid evaporates and condenses on the nearby solid surface, one condition for establishing an equilibrium contact angle is

that the newly formed solid–vapor interface also establishes an equilibrium energy γ_{sv}. Proving experimentally whether or not interfacial properties are reasonably equilibrated prior to contact angle measurement is problematic for many reasons including the fact that solid–vapor interfacial energies are not directly measureable. However, given that static contact angle measurements for similarly sized droplets are consistent in literature, it appears that most systems are either equilibrated or changing very slowly. Further discussions in this direction are beyond the scope of this review, but we feel that it is important to recognize the subtleties of even the simplest contact angle measurements. Here we treat the static contact angle defined by the Young equation as an observable quantity that is useful in characterizing the curvature of a phase boundary and associated normal surface stress, or Laplace pressure, on the liquid–fluid interface.

Below the capillary length scale, where surface forces dominate gravity, the near-spherical surface profile of a sessile droplet is maintained close to the contact line, and a tangent drawn at the intersection can be used to measure the contact angle (see Fig. 1(a)). However, the local curvature within the range of disjoining pressures (up to 1–100 nm for partially wetting droplets in vapor [39]) may deviate from the above-observed apparent contact angle due to effects including van der Waals forces, EDLs, molecular orientations and surface adsorption [39–42] — we have drawn attention to this range in the close-up view in Fig. 1(a). The complications associated with modeling the local contact angle were summarized well by Kang and Kang [43]. At the droplet scale, however, these local deviations or edge effects, at the contact line have a negligible effect on the overall surface energy minimum represented by θ_S. This reasoning is tentatively extended to many EWOD microfluidic systems, i.e., the electrical energy added to the system is mostly stored at the solid–liquid interface (in the dielectric layer, to be specific for EWOD configuration), and by accounting for the capacitance the apparent static contact angle under EWOD can be predicted *via* the electrowetting equation. If one looks at the interfaces very close to the triple line, however, the presence of an applied electric field will result in an added electrostatic component of disjoining pressure on the liquid–fluid interface, thereby affecting how the local, sub-microscopic, or true contact angle at the edge deviates from the energy-predicted macrosopic or apparent EWOD angle. This influence of the solid–fluid interface on the liquid–fluid interface, which is the root cause of the voltage-dependent contact angle in electrowetting, is discussed in the following section.

3.2. The Static Contact Angle under Electrostatic Forces by EWOD

Consider a conductive droplet in an ambient dielectric fluid sitting on a flat dielectric-coated electrode with a voltage applied between the liquid and the electrode, as shown in Fig. 1(b). Notice, in the close-up view, the tight curvature of the liquid–fluid interface below the length scale χ — this feature is predicted by electromechanical models of EWOD [44] and has been observed in experiments [45]. Such methods are discussed in this section as well as the theoretical arguments that

lead to the expectation that the microscopic true contact angle at the contact line in Fig. 1(b) is Young's angle (i.e., θ_S in Fig. 1(a)).

Assuming the liquid (refer to Fig. 1(b)) near the solid–liquid boundary possesses a net charge such that the field is completely screened from the interior of the liquid, every point on the liquid–solid interface will feel normal electrostatic force, i.e., downward force. Also, the fringe electric field at the rim of the droplet exerts electrostatic traction normal to the liquid–fluid boundary right above the contact line (i.e., within χ in the figure) and hence a net force in the direction parallel to the solid, causing droplet spreading. From this interpretation one may formulate an electromechanical problem without assuming that the solid–liquid interfacial tensions are changed by external voltage. For example, by integrating the Maxwell stress tensor over a control surface around the liquid–fluid boundary, Jones showed that total force per unit length of contact line is equal to $c_d V^2/2$, demonstrating a purely electromechanical derivation of the electrowetting equation [46]. Jones' derivation required no information about the actual shape of the liquid–fluid interface. Alternatively, by electrostatic analysis of a conducting wedge, Kang provided mathematical proof that the Maxwell stress causing spreading is localized to the contact line within a distance comparable to the dielectric thickness [47]. Using a more involved electrostatic analysis (discussed below) Buehrle *et al.* [44] predicted the actual shape of the meniscus near the contact line under EWOD. Use of the Maxwell stress tensor for calculating the various forces on conductive and dielectric liquid droplets is covered in depth by Zeng and Korsmeyer [48]. Before moving on to the details, let us note that earlier Vallet *et al.* [49] analyzed the electrostatic field near the droplet edge using conformal mapping, in light of their proposed air ionization mechanism for contact angle saturation.

If the goal is to model the local contact angle, the Maxwell stress tensor can be used, provided that it is incrementally solved at points along the liquid–fluid interface, as demonstrated by Buehrle *et al.* [44]. A notable challenge in determining the free surface profile f is that to solve the equation for mechanical equilibrium, a balance of Maxwell stress Π_e and Laplace pressure [45]

$$\Pi_e(\vec{r}) = \gamma\left(\frac{f''}{(1+f'^2)^{3/2}}\right), \tag{2}$$

requires a solution for the electrical field, which, in turn, depends on f. The vector $\vec{r}$ specifies a point on the surface s. Buehrle *et al.* [44] developed iterative technique to calculate equilibrium surface profiles near the contact line. An analytical model based on conformal mapping was used to yield similar results, although they were limited to relatively small voltages [50]. Investigations of the local surface profile have been instructive with respect to the expected electric field divergence at the contact line [49]. Interestingly, mathematical analyses have led to the expectation that the local contact angle approaches Young's angle, i.e., the static contact angle in the absence of an electric field, as the distance from the interface to the contact line approaches zero. Buehrle *et al.* [44] provide concise reasoning for this expectation,

paraphrased as follows: the electrostatic force (per unit length of contact line) F_e pulling the contact line is expressed by the limit

$$F_e \propto \lim_{\delta r \to 0} \int_0^{\delta r} \Pi_e(y)\, dy, \tag{3}$$

where y is the coordinate perpendicular to the solid surface. Electrostatic analysis leads to the conclusion that $\Pi_{el} \propto \delta r^{\nu}$ (with $-1 < \nu < 0$) around a conducting wedge. Equation (3) then leads to $F_e \propto \delta r^{\nu+1}$, meaning that the electrostatic force approaches zero as $\delta r \to 0$. In other words, the electrowetting force is not mathematically concentrated on the contact line.

Modeling the local contact angle under EWOD has led to many important insights, including the likely connection between the divergence of the electric field at the contact line and contact angle saturation and various device failure mechanisms. The length scale over which the electric field is expected to diverge from the contact line has been directly related to the dielectric thickness d [45, 49–51]. Mugele and Buehrle [45] presented a vivid experimental result showing that EWOD experiments can be designed such that the liquid–fluid interface increases its slope tightly from the EWOD contact angle to the Young's contact angle over an observable distance (e.g., ~100 μm) from the contact line. This distance, the authors expect, corresponds to a characteristic distance (indicated by χ in Fig. 1(b)) related to the dielectric thickness and relative permittivities of the solid and ambient fluid (in their case the fluid was oil). While this result has not been replicated with sessile droplets in air or vapor, a recent experiment by Gupta *et al.* [52] tracks capillary condensation in a nano-gap of a surface force apparatus under EWOD. Their results corroborate the electromechanical interpretations described above by showing that capillary condensation is unaffected by EWOD voltage in the nano-gap that is smaller than d, thereby suggesting that the liquid–solid interfacial tension is unchanged in EWOD. The differences between droplet-in-oil and droplet-in-air systems with respect to EWOD have yet to be fully characterized. It is well known among EWOD practitioners that an oil phase can fully encapsulate working droplets on hydrophobic solid surfaces such that the working droplets do not contact the solid surface until voltage is applied and pulls the more polarizable liquid to the solid surface. This process of oil entrapment and voltage-induced destabilization is characterized in a highly recommended report by Staicu and Mugele [53].

3.3. EWOD-Driven Droplet Translation — Free-Body Diagrams

In the literature, one may encounter various physical descriptions of how a droplet translates by an asymmetric EWOD actuation based on unbalanced electrostatic forces, surface tension forces or hydrostatic pressures [1, 12]. While each is based on a physically different mechanism, these descriptions should not be considered contradictory. In fact, altogether they can provide a richer understanding of EWOD-driven droplet motion. To illustrate this point, we present a set of free-body diagrams (FBDs) illustrating how a liquid droplet moves in a parallel-plate EWOD

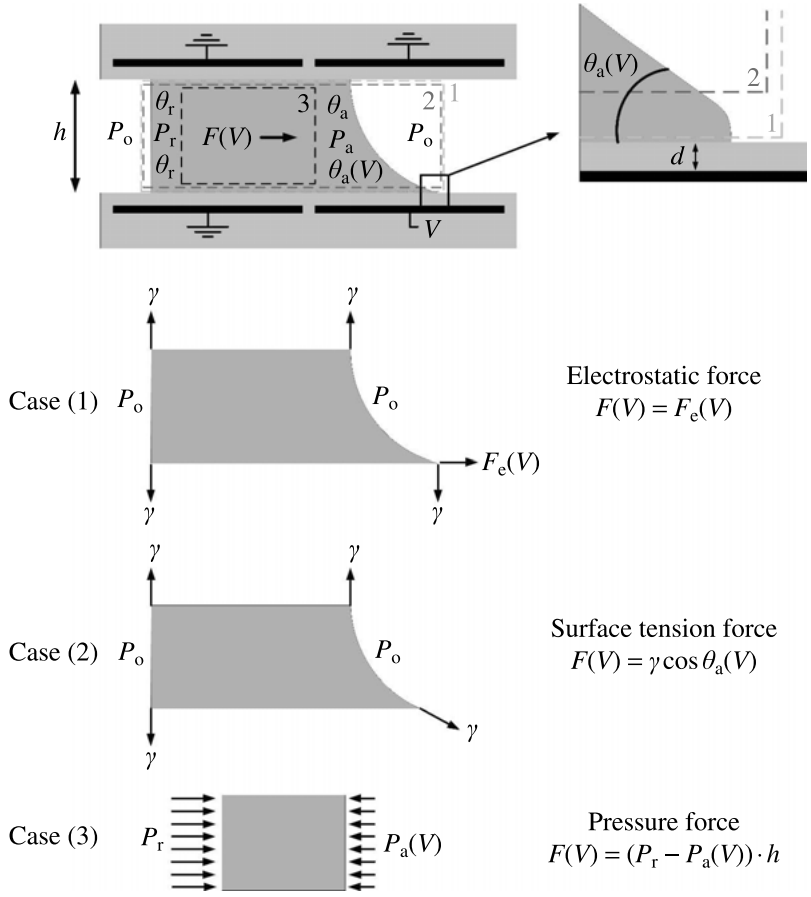

Figure 2. Cross section of EWOD droplet translation and free-body diagrams for Boxes 1, 2 and 3, corresponding to interpretations of driving force on the droplet $F(V)$ based on electrical, surface tension and pressure forces, respectively. The force is per unit width into the page.

device. Figure 2 gives a cross section of the typical actuation scenario. The droplet moves to the right while the lower right electrode is activated and all others are grounded. To simplify the situation and help focus on the active region, let us assume that the contact angle under zero voltage is 90° for both the advancing and receding cases. With voltage applied, the meniscus bends with a radius of curvature equal to $h/\cos\theta_a(V)$. The observed angle decreases to the EWOD angle $\theta_a(V)$ above χ from the solid surface, but Young's angle is maintained right on the solid surface.

Each FBD in Fig. 2 corresponds to a slightly different volume of the same droplet, as indicated by Box 1, 2 and 3. Case (1) shows the FBD of the liquid body enclosed by Box 1, which has its upper and lower boundaries mathematically right above the solid surface. For this case, the net force (in the direction of motion)

per unit length of the contact line (into the page) $F(V)$ is equal to the electrostatic force by the EWOD voltage V, i.e., $F(V) = F_e(V)$. With all contact angles equal to 90°, there is no net component of surface tension in the direction of motion. In contrast, the upper and lower boundaries of Box 2 are located a microscopic distance away (i.e., greater than χ) from the solid surface; there is no electrostatic force on this FBD. Case (2) in Fig. 2 shows the unbalanced components of liquid–fluid surface tension acting on the liquid body, leading to $F(V) = \gamma \cos\theta_a(V)$. Box 3 (black broken line) encloses a liquid volume entirely within the droplet; there is no electric field or surface tension on this FBD. Case (3) in Fig. 2 shows the unbalanced hydrostatic pressure acting on the liquid body. The driving force is expressed in terms of a pressure gradient extending from the receding to advancing ends of the droplet: $F(V) = [P_r - P_a(V)]h$. P_r is always larger than P_a because the curvatures of the opposing liquid–fluid interfaces are such that the Laplace pressure drop from the ambient pressure is always larger on the EWOD end. As expected, all three expressions for the EWOD driving force are interchangeable, e.g., $F(V) = F_e(V) = \gamma \cos\theta_a(V) = [P_r - P_a(V)]h$.

Having gone through the above exercise, we can see that different ways to understand how EWOD actuation drives a droplet may coexist. At the most fundamental level among the three, the electrostatic force by EWOD voltage pulls the droplet, making the apparent contact angle decrease in the process (Case (1) in Fig. 2). Given the decreased contact angle (whatever the cause was), we should conclude that the decreased slope of the liquid–fluid interface on the EWOD end pulls the droplet forward. At the same time, we see that the reduced contact angle has changed the liquid–fluid curvature to increase the Laplace pressure drop from the ambient (Case (2) in Fig. 2). Following a similar argument, given the lower pressure on the EWOD side inside the droplet, we should conclude that the liquid on the non-EWOD end flows toward the low-pressure region on the EWOD end (Case (3) in Fig. 2). Depending on the application, one method may be more convenient than others. For example, to understand the flow distribution inside an EWOD-driven droplet, the pressure interpretation is likely the most useful.

4. EWOD Circuit Models

4.1. Lumped Elements

Electrical circuit models are useful in predicting the behavior of EWOD systems below the contact angle saturation limit, which is not covered in this review. In general, every material in the EWOD device can be approximated by a leaky dielectric and represented in a circuit by a resistor and capacitor in parallel. Because the droplet is typically several orders of magnitude more conductive than the confining solid dielectric layers and the surrounding dielectric fluid, resistances of the latter materials are considered infinite. The circuit shown in Fig. 3 represents a sim-

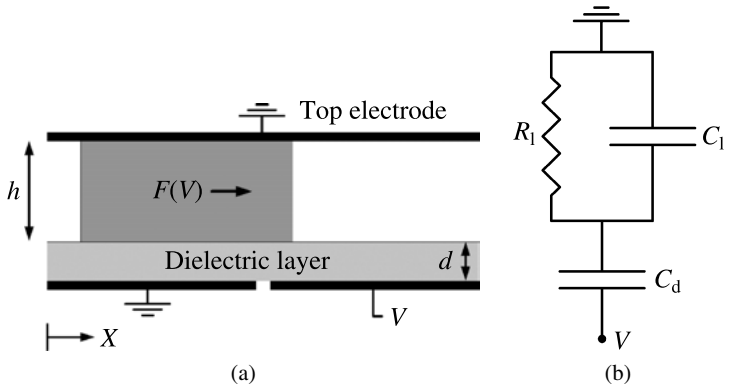

Figure 3. (a) A parallel-plate EWOD configuration in side view. The lower plate is a substrate with dielectric (of thickness d) and bottom electrodes. The upper plate has a top electrode and is separated by a distance h from the lower plate. A liquid droplet is squeezed between the plates. (b) Simplified circuit diagram of a droplet and a dielectric layer in series between top and bottom electrodes.

plified EWOD circuit model. For a fixed applied voltage $V = V_{\text{top}} - V_{\text{bottom}}$, the electrical 'coenergy' is [54]

$$E^* = \int_0^V C_{\text{EQ}}(x) U \, \mathrm{d}U = \frac{1}{2} C_{\text{EQ}}(x) V^2, \tag{4}$$

where $C_{\text{EQ}}(x)$ is the equivalent capacitance, which varies spatially according to the location x of the moving droplet. The force driving EWOD motion is

$$F = \frac{\mathrm{d}E^*}{\mathrm{d}x} = \frac{V^2}{2} \frac{\mathrm{d}C_{\text{EQ}}(x)}{\mathrm{d}x}. \tag{5}$$

In most reported analyses, the effect of contact angle on $C_{\text{EQ}}(x)$ is small and is therefore ignored. EWOD circuit models have become very common in EWOD force analyses, most notably by Jones [46, 55–57] for height-of-rise systems and more recently in works specific to digital EWOD geometries by Baird *et al.* [58], Young and Mohseni [59], Kumari *et al.* [60], Bahadur and Garimella [61], Chatterjee *et al.* [62] and Fan *et al.* [31]. As stated by Jones [46, 63], a key benefit of this approach beyond its simplicity is that it allows one to incorporate the relevant frequency dependences (i.e., arising from complex permittivities) into the force equation.

4.2. Electrical Time Scales

Two important time scales associated with the movements of electrical charges in EWOD actuation are the charging time of the solid–liquid interface τ_{charge} and the period of the applied voltage τ_{applied}. If $\tau_{\text{charge}} \ll \tau_{\text{applied}}$, the liquid phase boundary will acquire a net charge while voltage is applied, shielding the liquid bulk from the electric field. In this case of a net charge on the liquid surface, the electrostatic forces exerted by fringe fields will cause spreading near the contact line.

Alternatively, if $\tau_{\text{charge}} \gg \tau_{\text{applied}}$, the liquid phase boundary will *not* acquire a net charge as quickly as the voltage is applied, and the electric field will be distributed within the liquid bulk phase. In general, one can predict the direction of each component of electrical force based on a simple principle: the droplet will move in the direction that maximizes the amount of capacitive energy that can be stored in the EWOD circuit.

The charging time τ_{charge} is basically the RC time constant for the circuit that powers the EWOD device, in which the liquid and dielectric layers can be modeled as resistive and capacitive elements, respectively, as shown in Fig. 3(b). The droplet and dielectric layers are modeled as a parallel resistor and capacitor (for the droplet) in series with another capacitor (for the dielectric layer). In most cases the capacitance of EDL is not included in the analysis because it is likely to be much higher than that of the dielectric layer [64–66]. The cases for which the EDL should be included in the analysis are discussed in Section 4.3. Assuming we have applied a DC voltage across the circuit elements shown in Fig. 3(b), the associated charging time is [55]

$$\tau_{\text{charge}} = R_{\text{l}}(C_{\text{l}} + C_{\text{d}}) = \frac{\varepsilon_{\text{o}}}{\sigma_{\text{l}}}\left(\varepsilon_{\text{l}} + \frac{h}{d}\varepsilon_{\text{d}}\right). \tag{6}$$

Here, R_{l} is the resistance of the liquid droplet, σ_{l} is the conductivity of the liquid, and C_{l} and C_{d} are the capacitances of the liquid and dielectric layers, respectively. In this simple model the droplet poses the only significant resistance to current flow for charging and discharging, but in reality the EWOD circuit likely has other sources of resistance that may affect the charging time.

The inverse of charging time can be used to define a critical actuation frequency f_{c}, at which $\tau_{\text{charge}} = \tau_{\text{applied}}$ or $\omega_{\text{c}} = 2\pi f_{\text{c}} = 1/\tau_{\text{charge}}$. Many researchers have distinguished the low and high frequency actuation regimes (i.e., $f \ll f_{\text{c}}$ and $f \gg f_{\text{c}}$) by saying that EWOD forces are in play while operating in the former because the electric field is formed only in the dielectric layer (neglecting the fringe field at the contact line), whereas operating in the latter will summon a DEP force based on the redistribution of the electric field through the droplet [46, 55–57, 62, 67]. Chatterjee *et al.* [62] demonstrated that for typical device dimensions and increasing frequency, this redistribution of forces (i.e., EWOD and DEP) can result in a highly diminished total force. Accuracy of the terms aside, the distinctions above are simple ways to characterize the field distribution in the chip, and many researchers find it helpful to distinguish between EWOD and DEP forces. Fan *et al.* [31] provide an elegant demonstration of actuating both aqueous and dielectric fluids, using AC and DC voltages, respectively, on a single chip. Previously, Chatterjee *et al.* [67] reported the feasibility of moving nonaqueous solvents and solutions at various frequencies and device dimensions. The frequency-dependent field distribution in sessile droplet under EWOD is illustrated well in a recent report by Lee *et al.* [68]. In Fig. 4, their simulations of electric field show that increasing the applied frequency not only results in a field within the droplet, but also the disappearance of

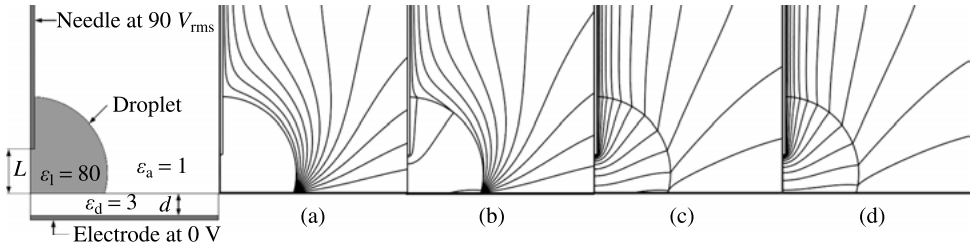

Figure 4. Potential distributions for $V_{rms} = 90$ V, $L = 0.58$ mm, $t_d = 5$ μm, and droplet electrolyte concentration of 0.1 mM (liquid conductivity = 1.8 mS/m). The contour interval is 10 V. Reproduced with permission from Lee *et al.* [68]. L is the vertical distance between the tip of the needle and the top surface of the dielectric. (a) dc, (b) $f = 10$ kHz, (c) $f = 100$ kHz, (d) $f = 1$ MHz.

the field intensification at the contact line. For this case, the critical frequency according to $f_c = 1/(2\pi\tau_{charge})$ and equation (6) is $f_c \sim 85$ kHz, above which the electrical field at the contact line is highly diminished.

4.3. The Electrical Double Layer

Even with no applied potentials, a solid surface acquires a net charge density due to chemical adsorption and ionization or dissociation of surface groups. Consequently, when in contact with a liquid containing mobile ions, the liquid near the solid also acquires a net charge density of opposite polarity, forming an EDL with the associated electrical potential ψ and characteristic length λ_D, the Debye length. Further, we discuss EDL in terms of two quantities relevant to electrowetting: static contact angle θ_S and double layer capacitance C_{EDL}.

At distances from the contact line less than λ_D, both the liquid–fluid interfacial energy and curvature are affected by the charge distribution in the EDL, which is itself affected by the geometry of the interface. It is instructive to step through a simple derivation of the one-dimensional linearized Poisson–Boltzmann equation in order to see the relevance of λ_D. For a charged solid surface in contact with a liquid, the charge density follows the Poisson equation,

$$\nabla^2\psi = \frac{d^2\psi}{dy^2} = \frac{-\rho_E}{\varepsilon}, \tag{7}$$

where y is the coordinate normal to the solid (at which $y = 0$), ρ_E is the charge density (C/m^3) and ε is the permittivity of the liquid. Boltzmann statistics provides a way to describe the concentration n_i of species i having valence z_i at a given potential ψ as a function of electrostatic and thermal energies

$$n_i = n_{i\infty}\exp(-z_i e\psi/k_B T), \tag{8}$$

where e is the charge of an electron and $n_{i\infty}$ is the bulk concentration far from the surface. With the charge density given by $\rho_E = \sum z_i n_i e$, equations (7) and (8) are combined to form the one-dimensional Poisson–Boltzmann equation,

$$\frac{d^2\psi}{dy^2} = -\frac{e}{\varepsilon}\sum_i z_i n_{i\infty}\exp(-z_i e\psi/k_B T). \tag{9}$$

The assumption that $z_i e\psi \ll k_B T$ (~25 mV at room temperature) constitutes the Debye–Hückel approximation and leads to a linearized version [69],

$$\frac{d^2\psi}{dy^2} = \lambda_D^{-2}\psi. \tag{10}$$

Here we have inserted λ_D, which is defined as

$$\lambda_D = \left[(e^2/\varepsilon k_B T) \sum_i z_i^2 n_{i\infty} \right]^{-1/2}. \tag{11}$$

With boundary conditions $\psi(y = 0) = \psi_o$ and $\psi(y \to \infty) = 0$, the exponential solution $\psi = \psi_o \exp(-y/\lambda_D)$ indicates that λ_D provides an approximate measure of the EDL and therefore a distance from the solid surface below which contact angle measurements may be influenced by ψ. Based on this simplified result, a symmetric electrolyte having bulk concentration of molarity M has $\lambda_D \approx 3 \times 10^{-10}|z|^{-1}M^{-1/2}$ (m) [69]. For example, at room temperature, deionized water ($M \sim 10^{-7}$) has $\lambda_D \sim 1$ μm, and a salt solution with $M \sim 10^{-1}$ has $\lambda_D \sim 1$ nm. In most cases the EDL will not affect the observed θ_S, because the λ_D is much smaller than the measurement resolution and the radius of the droplet. The specifics of EDL modeling near the contact line are beyond the scope of this review; we recommend the mathematical investigations of Chou [40] and Kang and coworkers [43, 70], which employ various forms of the Poisson–Boltzmann equation to calculate charge distributions within the liquid phase(s).

The simplest, albeit roughest, way to predict how the presence of EDLs influences the total electrical force on a droplet is by EWOD circuit analysis with capacitive elements representing EDLs. Figure 5 shows a simple two-dimensional EWOD configuration and corresponding circuit model. We have chosen to let the resistance of the bulk droplet go zero (i.e., $R_l \to 0$) and the device dielectric layers and EDLs have infinite resistance. The applied voltage V is fixed, and V_1,

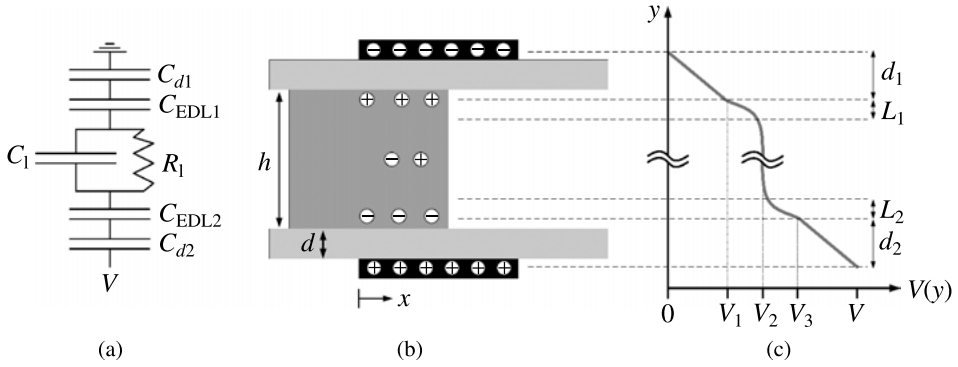

Figure 5. The effect of the EDL in a circuit model of EWOD: (a) circuit model of the liquid and solid dielectric layers, (b) liquid sandwiched between dielectric layers and electrodes, and (c) qualitative plot of electrical voltage *versus* y-location.

V_2 and V_3 depend on the capacitances per unit width (into the page) of the upper dielectric ($C_{d1} = \varepsilon_o \varepsilon_d x/d_1$), lower dielectric ($C_{d2} = \varepsilon_o \varepsilon_d x/d_2$), upper EDL ($C_{EDL1} = \varepsilon_o \varepsilon_e x/L_1$) and lower EDL ($C_{EDL2} = \varepsilon_o \varepsilon_e x/L_2$). The total EWOD force, neglecting fringe capacitance and assuming $d \ll h$, is

$$F_x = \frac{dE^*}{dx} = \frac{V^2}{2}\frac{dC_{EQ}(x)}{dx} \approx \frac{\varepsilon_o V^2}{2}\left(\frac{d_1 + d_2}{\varepsilon_d} + \frac{L_1 + L_2}{\varepsilon_{EDL}}\right)^{-1}, \tag{12}$$

in which the equivalent capacitance of the circuit is

$$C_{EQ} = \left(\frac{1}{C_{d1}} + \frac{1}{C_{d2}} + \frac{1}{C_{EDL1}} + \frac{1}{C_{EDL2}}\right)^{-1}. \tag{13}$$

Note that equation (12) represents the actuation force of conventional electrowetting (directly on conductor with no insulation layer) [1] when $d_1 = d_2 = 0$. This lumped elements analysis leads to the same result given by analyses based on the linearized Poisson–Boltzmann equation given by Hua *et al.* [66] and Mugele and Baret [65], who stated the result in terms of a corrected electrowetting number,

$$Ew_{corr} = Ew \cdot \left(\frac{1}{1 + \varepsilon_d \lambda_D/\varepsilon_{EDL} d}\right). \tag{14}$$

Note that treatments based on EDL models do not model variations of interfacial tension, but rather the EDL charge distribution results in an osmotic pressure that is added to the electrostatic force [71]. Since the Debye–Hückel approximation, i.e., $z_i e\psi \ll 25$ mV, leads to equation (14), it is useful to go back to our circuit analysis to estimate the EDL potentials to see if the initial assumption was appropriate. For example, at room temperature, deionized water ($M \sim 10^{-7}$) has $\lambda_D \sim 1$ μm, and $(V_3 - V_1)/2 \approx 200$ mV. On the other hand, a salt solution with $M \sim 10^{-1}$ has $\lambda_D \sim 1$ nm, and $(V_3 - V_1)/2 \approx 200$ μV. In both cases, we used $d_1 = d_2 = 1$ μm, $\varepsilon_d = 3$ and $\varepsilon_E = 80$, which are common to reported aqueous solution EWOD devices. For this analysis, which neglects fringe fields, the Debye–Hückel approximation is questionable for low conductivity liquids and acceptable for most electrolyte solutions, for which the EDL capacitance is very high and makes a negligible contribution to the total force.

5. EWOD Hydrodynamics

EWOD actuation is a multi-scale, multi-stage process, in which the following events take place upon the application of voltage: (i) electrical charges reorient and/or migrate, establishing an electric field in response to the applied voltage, (ii) the liquid in the vicinity of the advancing contact line moves, and (iii) the entire droplet moves. Stage (ii) is often described as the 'stretching', because the droplet elongates in the direction of motion before the rear contact line moves. The purpose of this section is to provide a survey of popular modeling and experimental techniques for investigating droplet and contact line motions. Each subsection will begin

by introducing the theoretical framework of each approach and finish by discussing how the models and/or methods have been adapted to incorporate electrowetting.

5.1. Steady Droplet Motion

The motion of a droplet sliding on or between planar surfaces, e.g., the droplet in Fig. 1 or 2, poses a number of interesting challenges to those who wish to model its flow by using standard fluid mechanics equations. Namely, a faithful model cannot be expected without proper boundary conditions, which in the case of sliding droplets must incorporate contact line wetting and dewetting dynamics. Neither process is fully understood, nor has the influence of electrowetting been clarified. In spite of this, velocity-dependent relationships for drag originating at or near the contact line have been constructed through the use of hydrodynamic and atomistic models, each with the necessary empirical fitting parameters.

In their analysis of a proposed electrowetting-based display, Beni and Tenan [25] used a one-dimensional Poiseuille flow solution for a liquid slab between two semi-infinite parallel plates with air as the surrounding medium. By balancing the driving force $\Delta\gamma_{sl}$, which is the assumed voltage-induced change in solid–liquid interfacial tension (that can be represented by γEw), and drag terms, they arrive at a simplified equation for steady-state velocity:

$$v = \frac{\Delta\gamma_{sl} - \alpha}{s\mu\lambda + \beta} \quad \text{or} \quad Ca = \frac{Ew - \alpha/\gamma}{s\lambda + \beta/\mu}. \tag{15}$$

A shape factor s accounts for the channel geometry, μ is the dynamic viscosity, λ is the ratio of slab length and height, Ca is the capillary number ($Ca = v\mu/\gamma$), and β is a proposed coefficient of viscosity for the contact line. They stressed the importance of α, the static component of contact line friction force per unit length, because (i) it determines the threshold electrowetting force for movement and (ii) its dependences on system parameters (e.g., contact angle, voltage, etc.) are not sufficiently understood.

In modeling a similar scenario to that described above, Ren *et al.* [72] compiled force terms related to EWOD, contact line friction, and viscous drag in order to derive a steady-state velocity equation. It is worth noting that they inserted a term derived from hydrodynamic theory that accounts for viscous dissipation near the contact line (which is allowed to slip [73]) and a term that reflects a linear dependence of contact line viscosity (like β), which they attributed to the low-speed regime of the molecular-kinetic theory (MKT) [74, 75]. The use of two distinct theoretical approaches reflects the unresolved state of wetting theory, which is central to understanding the dynamics of EWOD actuation. Subsequently, more advanced models have been proposed for squeezed droplet scenarios [76–83]. A common feature is that static and dynamic contact angle drag terms are based on experimental data rather than theoretical models. The numerical treatments of Walker *et al.* [78] and Lu *et al.* [79] demonstrate excellent agreement between experimental and predicted droplet shapes during movement, splitting and merging in the

parallel-plate geometry. Importantly, if the gap between the parallel plates is much smaller than the disc diameter of the droplet between the plates, the droplet is correctly approximated as a Hele-Shaw cell [77–79], in which the flow is treated as two-dimensional. This is clearly not the case for sessile droplets, which exhibit complex three-dimensional flow patterns owing to the spherical shape and large free surface area [84]. In fact, the ability to efficiently induce mixing within sessile droplets by applying fields through EWOD has been reported [85–87].

5.2. *Steady Contact Line Motion*

The three-phase contact line poses a specific challenge in modeling the wetting process: the traditional 'no-slip' boundary condition of continuum analysis leads to the unrealistic expectation of infinite stress at the singular triple point. Modeling the advancement of the contact line by fluid mechanics therefore requires a special boundary condition. Classically, this has been accomplished by either excluding a small region around the triple point from the analysis [88, 89] or relaxing the no-slip boundary condition [90–92].

Bavière *et al.* [93] compared velocities of droplets sliding on a planar surface by EWOD actuation with the velocity predicted by Brochard's model [88] for a droplet moving along a solid–liquid interfacial tension gradient. This comparison is particularly instructive with respect to the reasons that certain observations and theoretical predictions are *dissimilar*. Brochard's model is built upon the assumption that the dominant energy dissipation mechanism of spreading is viscous shear within a sharp wedge of liquid near the moving contact line [94]. 'Sharp' means that the dynamic contact angle $\theta_D \ll 1$ rad, so that the lubrication approximation is valid. With small angles, the steady-state velocity under EWOD actuation is given by [88, 93, 95]

$$v = \frac{\gamma}{\mu}\frac{\theta_D}{6n}(Ew - \alpha/\gamma) \quad \text{or} \quad Ca = \frac{\theta_D}{6n}(Ew - \alpha/\gamma). \tag{16}$$

Here, n is the logarithmic of macroscopic over microscopic length such that n is typically ~ 10 [95, 96]. In the experiments of Baviere *et al.* [93], all contact angles were > 1 rad, as is standard for EWOD because of the requirement for low-hysteresis surfaces, e.g., Teflon®. It is expected that the lack of a sharp wedge will result in comparatively low viscous dissipation near the contact line, begging the question: what is the dominant mechanism? Velocity-dependent contact angle hysteresis was observed in droplets at $Re > 100$ (Re: Reynolds number $= vL\rho/\mu$, where L is the characteristic length scale and ρ is the fluid density). Additionally, Baviere *et al.* [93] propose that an atomistic approach such as the MKT may better describe contact line dynamics for high θ, high Re EWOD actuation. It is also important to note that other hydrodynamic formulations, e.g., those of Cox [92] and Voinov [89], are perhaps more applicable to higher static and dynamic contact angles. Importantly, these models predict that there is a region above the contact line over which the curvature of the liquid–fluid interface drastically changes (re-

ferred to as 'viscous bending' [96]) from a microscopic local angle to the observed apparent dynamic angle [97].

The MKT is based on the supposition that molecular adsorption and desorption at the contact line are the dominant dissipation mechanisms in wetting [98]. The movements of liquid molecules from the liquid surface to the dry solid surface and *vice versa* can be characterized by hopping rates $+k$ and $-k$, respectively. Further, at equilibrium (i.e., a stationary contact line), $+\kappa = -\kappa = \kappa^0 \sim k_B T e^{-Wa}/\mu q$ [96], a function proportional to the Boltzmann constant k_B, absolute temperature T, and the exponential of work of adhesion between the liquid and solid W_a. Incidentally, κ^0 is inversely proportional to the molecular flow volume q and bulk viscosity μ. By way of the Eyring–Frenkel theory of liquid transport [99, 100], the relationship between contact-line speed and static θ_S and dynamic advancing θ_D contact angles is [74]

$$v = 2\kappa^0 \lambda \sinh\left[\gamma(\cos\theta_S - \cos\theta_D)\lambda^2/2k_B T\right]. \tag{17}$$

The driving force of wetting is a result of non-equilibrium contact angle, and λ represents the molecular hopping distance. To incorporate EWOD into this model, Blake *et al.* [101] inserted voltage-dependent contact angles, $\theta_S(V)$ and $\theta_D(V)$. In a recent study by Yuan and Zhao [102], the MKT is employed with molecular dynamics simulations to investigate the propagation of precursor films in electrowetting. Their work demonstrates the potential of atomistic approaches in solving fundamental questions in wetting mechanisms.

Note that at low velocities, equation (17) is approximately linear, providing the rationale for inclusion of a linear term in the velocity equation of Ren *et al.* [72]. The linear version allows one to state the capillary number as

$$Ca = (\cos\theta_S - \cos\theta_D(V) + Ew)\frac{\lambda^3 e^{-Wa}}{q}. \tag{18}$$

Figure 6 [96] provides a visual comparison of the hydrodynamic and atomistic models. In the hydrodynamic case (Fig. 6(a)), it is assumed that the observed dynamic

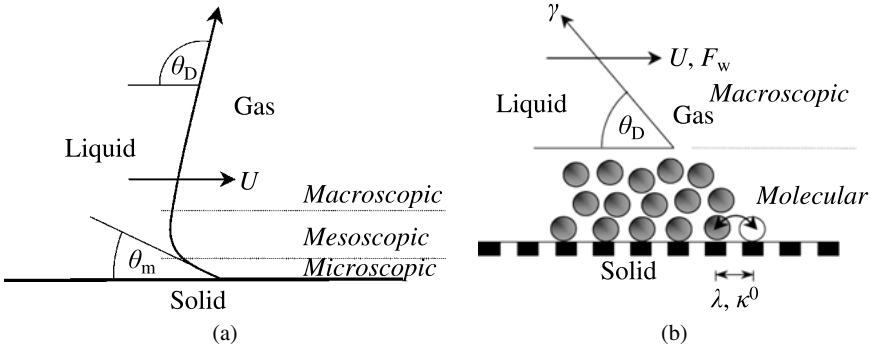

Figure 6. Models of wetting: (a) viscous bending on the mesoscale for an advancing meniscus, and (b) dynamic wetting according to the molecular-kinetic theory. Reproduced with permission from Blake [96].

advancing contact angle θ_D deviates from the static equilibrium contact angle θ_S (or microscopic angle θ_m in the figure) [89] because of viscous dissipations related to flow in a region near the contact line, which was divided into 'macroscopic', 'mesoscopic' and 'microscopic' length scales. In contrast, the MKT (Fig. 6(b)) attributes dynamic drag to the energy used by molecules hopping around the contact line. At low *Ca*, which is likely to apply to EWOD actuation, this can lead to an apparent viscosity associated with the contact line ($\approx \mu q e^{Wa}/\lambda^3$). In contrast, viscous dissipation in the hydrodynamic view is a function of geometry near the contact line, predicting strong viscous drag at the contact line when the static (or microscopic) contact angle is low. In EWOD of aqueous liquids, however, measured contact angles are relatively high, and there is unlikely to be a precursor film [42, 103]. It is likely that different mechanisms dominate in different flow regimes (θ, *Ca*, etc.), a notion supported by the finding that combined models are robust [96, 104]. Paneru *et al.* [105] have recently explored the applicability of hydrodynamic and molecular-kinetic models for EWOD droplet spreading of ionic liquids immersed in oil. With respect to EWOD, the effects of electric fields on the local properties of the moving contact line will complicate the process of developing the right model(s).

5.3. Unsteady Motion

The various types of droplet oscillations that can accompany AC EWOD actuation have led to interesting experiments [86, 106, 107] as well as novel device demonstrations, such as droplet mixers [85], micro-bubble tweezers [108], and a wiper-free windscreen [109]. At sufficiently low frequencies EWOD voltage can excite capillary waves that drive vortices inside the droplet [86]. High frequency actuation leads to circulatory flow that has been attributed to electrothermal phenomena [68, 106] related to the electrical field penetrating the droplet. Malk *et al.* [110] provide an interesting report with videos on EWOD droplet oscillations up to 3 kHz. Sen and Kim [111] provide clear analyses of sessile droplet spreading in response to step and low frequency actuations. More recently, Oh *et al.* [112] reported a rigorous mathematical model for unsteady droplet dynamics under EWOD actuation.

Li and Mugele [113] made the crucial observation that sessile droplets actuated in air using AC EWOD exhibit a significantly reduced contact angle hysteresis compared with droplets under DC voltage. This type of drag reduction was attributed to local oscillations of the droplet interface near the contact line, occurring over length scales below the measurement resolution and at frequencies matching the applied frequencies (0.2–10 kHz). This finding, which has implications for lowering driving voltage requirements in virtually all droplet-in-air EWOD devices, was reinforced by another recent study demonstrating a wiper-free windscreen that utilizes AC EWOD to facilitate droplet sliding down an inclined plane [109].

6. Summary and Conclusions

After briefly explaining the theoretical progression from electrocapillarity to the electrowetting equation and summarizing the development of the basic EWOD technologies, we provided systematic descriptions of the basic physics of EWOD and droplet actuation by EWOD. Motivation for this review was our ambition to bring together various interpretations of EWOD droplet actuation on a common ground so that the reader may form a clear picture of the fundamentals. For this purpose, we have developed an FBD analysis encompassing all the existing interpretations. Following the basic physics, we have reviewed various modeling efforts — electromechanics of EWOD actuation and hydrodynamics of EWOD-driven droplet motions — in order to strengthen the understanding and also reveal the limitations of the current knowledge. The simple models of EWOD droplet actuation presented here are excellent starting points for design and analysis of EWOD-based microfluidic devices. That said, it is our hope this review will inspire new research into the less understood EWOD regimes, for which the simple models fail to capture the droplet response. For example, saturation of the apparent contact angle at high *Ew* is not predicted by the electrowetting equation, but it has been observed in every reported EWOD experiment to date. This phenomenon has been attributed to a wide range of causes [51], most of which are failure mechanisms associated with high electric fields (e.g., dielectric charging and breakdown).

Acknowledgements

This work was supported by the NIH (R01 RR020070), DOE (DE-SC0005056), and the UCLA Foundation from a donation made by Ralph & Marjorie Crump for the UCLA Crump Institute for Molecular Imaging. WN acknowledges further supports from the NSF Graduate Research Fellowship Program and an NSF Integrative Graduate Education and Research Traineeship (IGERT) through the UCLA Materials Creation Training Program (MCTP).

References

1. J. Lee, H. Moon, J. Fowler, T. Schoellhammer and C.-J. Kim, *Sensors Actuators A* **95**, 259–268 (2002).
2. B. Berge, *Hebd. Seances Acad. Sci., Ser. B* **317**, 157–163 (1993).
3. J. Lee, Microactuation by continuous electrowetting and electrowetting: theory, fabrication, and demonstration, *PhD Thesis*, University of California, Los Angeles, 2000.
4. M. G. Pollack, R. B. Fair and A. D. Shenderov, *Appl. Phys. Lett.* **77**, 1725–1726 (2000).
5. Z. Hua, J. L. Rouse, A. E. Eckhardt, V. Srinivasan, V. K. Pamula, W. A. Schell, J. L. Benton, T. G. Mitchell and M. G. Pollack, *Anal. Chem.* **82**, 2310–2316 (2010).
6. R. Sista, Z. Hua, P. Thwar, A. Sudarsan, V. Srinivasan, A. Eckhardt, M. G. Pollack and V. K. Pamula, *Lab Chip* **8**, 2091–2104 (2008).
7. V. N. Luk and A. R. Wheeler, *Anal. Chem.* **81**, 4524–4530 (2009).
8. H. Moon, A. R. Wheeler, R. L. Garrell, J. A. Loo and C.-J. Kim, *Lab Chip* **6**, 1213–1219 (2006).

9. S. Chen, P. Y. Keng, R. M. van Dam and C.-J. Kim, in: *Proc. IEEE Int. Conf. MEMS*, Cancun, Mexico, pp. 980–983 (2011).
10. G. Lippmann, *Ann. Chim. Phys.* **5**, 494–549 (1875).
11. G. Beni, S. Hackwood and J. L. Jackel, *Appl. Phys. Lett.* **40**, 912–914 (1982).
12. G. Beni and S. Hackwood, *Appl. Phys. Lett.* **38**, 207–209 (1981).
13. J. Lee and C.-J. Kim, *J. Microelectromech. Syst.* **9**, 171–180 (2000).
14. C.-J. Kim, in: *Proc. 30th AIAA Fluid Dynamics Conference*, Norfolk, VA, USA (1999), Paper No. AIAA 99-380.
15. J. Crassous, C. Gabay, G. Liogier and B. Berge, *Proc. SPIE* **5639**, 143–148 (2004).
16. R. A. Hayes and B. J. Feenstra, *Nature* **425**, 383–385 (2003).
17. J. Heikenfeld and A. J. Steckl, *Appl. Phys. Lett.* **86**, 151121–151124 (2005).
18. H. Kang and J. Kim, in: *Proc. Int. Conf. MEMS*, Istanbul, Turkey, pp. 742–745 (2010).
19. P. Sen and C.-J. Kim, *J. Microelectromech. Syst.* **18**, 174–185 (2009).
20. J. Gong, G. Cha, Y. S. Ju and C.-J. Kim, in: *Proc. IEEE Int. Conf. MEMS*, Tucson, AZ, pp. 848–851 (2008).
21. A. G. Banpurkar, K. P. Nichols and F. Mugele, *Langmuir* **24**, 10549–10551 (2008).
22. W. Nelson, P. Kavehpour and C.-J. Kim, in: *Proc. Int. Conf. MEMS*, Hong Kong, China, pp. 75–78 (2010).
23. A. G. Banpurkar, M. H. G. Duits, D. van den Ende and F. Mugele, *Langmuir* **25**, 1245–1252 (2009).
24. M. Vallet, B. Berge and L. Vovelle, *Polymer* **37**, 2465–2470 (1996).
25. G. Beni and M. A. Tenan, *J. Appl. Phys.* **52**, 6011–6015 (1981).
26. A. A. Darhuber and S. M. Troian, *Annu. Rev. Fluid. Mech.* **37**, 425–455 (2005).
27. H. Dahms, *J. Electrochem. Soc.* **116**, 1532–1534 (1969).
28. H. Moon, S.-K. Cho, R. L. Garrell and C.-J. Kim, *J. Appl. Phys.* **92**, 4080–4087 (2002).
29. H. Moon and C.-J. Kim, in: *Microfluidic Technologies for Miniaturized Analysis Systems*, S. Hardt and Schönfeld (Eds), Springer, pp. 203–239 (2007).
30. D. Brassard, L. Malic, F. Normandin, M. Tabrizian and T. Veres, *Lab Chip* **8**, 1342–1349 (2010).
31. S.-K. Fan, T.-H. Hsieh and D.-Y. Lin, *Lab Chip* **9**, 1236–1242 (2009).
32. Y. Zhao and S.-K. Cho, *Lab Chip* **7**, 273–280 (2007).
33. H. A. Pohl, *J. Appl. Phys.* **22**, 869–871 (1951).
34. J.-C. Baret and F. Mugele, *Phys. Rev. Lett.* **96**, 016106–016110 (2006).
35. S. K. Cho, H. Moon and C.-J. Kim, *J. Microelectromech. Syst.* **12**, 70–80 (2003).
36. L. Minnema, H. A. Barneveld and P. D. Rinkel, *IEEE Trans. Elec. Insul.* **EI-15**, 461–472 (1980).
37. E. Colgate and H. Matsumoto, *J. Vac. Sci. Technol. A* **8**, 3625–3633 (1990).
38. M. Washizu, *IEEE Trans. Ind. Appl.* **34**, 732–737 (1998).
39. V. M. Starov, *Adv. Colloid Interface Sci.* **161**, 131–152 (2010).
40. T. Chou, *Phys. Rev. Lett.* **87**, 106101–106105 (2001).
41. V. M. Starov and M. G. Velarde, *J. Phys.: Condens. Matter* **21**, 464121–464132 (2009).
42. P.-G. de Gennes, *Rev. Mod. Phys.* **57**, 827–863 (1985).
43. K. H. Kang and I. S. Kang, *Langmuir* **19**, 9962–9967 (2003).
44. J. Buehrle, S. Herminghaus and F. Mugele, *Phys. Rev. Lett.* **91**, 086101–086105 (2003).
45. F. Mugele and J. Buehrle, *J. Phys.: Condens. Matter* **19**, 375112–375132 (2007).
46. T. B. Jones, *Langmuir* **18**, 4437–4443 (2002).
47. K. H. Kang, *Langmuir* **18**, 10318–10322 (2002).
48. J. Zeng and T. Korsmeyer, *Lab Chip* **4**, 265–277 (2004).
49. M. Vallet, M. Vallade and B. Berge, *Eur. Phys. J. B* **11**, 583–591 (1999).

50. M. Bienia, M. Vallade, C. Quilliet and F. Mugele, *Europhys. Lett.* **74**, 103–109 (2006).
51. F. Mugele, *Soft. Matter* **5**, 3377–3384 (2009).
52. R. Gupta, G. K. Olivier and J. Frechette, *Langmuir* **26**, 11946–11950 (2010).
53. A. Staicu and F. Mugele, *Phys. Rev. Lett.* **97**, 167801–167805 (2006).
54. S. Senturia, *Microsystem Design*. Kluwer Academic Publishers (2004).
55. T. B. Jones, J. D. Fowler, Y. S. Chang and C.-J. Kim, *Langmuir* **19**, 7646–7651 (2003).
56. K.-L. Wang and T. B. Jones, *J. Micromech. Microeng.* **14**, 761–768 (2004).
57. T. B. Jones and K.-L. Wang, *Langmuir* **20**, 2813–2818 (2004).
58. E. Baird, P. Young and K. Mohseni, *Microfluid. Nanofluid.* **3**, 635–644 (2007).
59. P. M. Young and K. Mohseni, *J. Fluid Eng. — Trans. ASME* **130**, 081603–081612 (2008).
60. N. Kumari, V. Bahadur and S. V. Garimella, *J. Micromech. Microeng.* **18**, 085018–08527 (2008).
61. V. Bahadur and S. V. Garimella, *J. Micromech. Microeng.* **16**, 1494–1503 (2006).
62. D. Chatterjee, H. Shepherd and R. L. Garrell, *Lab Chip* **9**, 1219–1229 (2009).
63. T. B. Jones, *Mech. Res. Commun.* **36**, 2–9 (2009).
64. B. Shapiro, H. Moon, R. L. Garrell and C.-J. Kim, *J. Appl. Phys.* **93**, 5794–5811 (2003).
65. F. Mugele and J.-C. Baret, *J. Phys.: Condens. Matter* **17**, 705–774 (2005).
66. C. K. Hua, I. S. Kang, K. H. Kang and H. A. Stone, *Phys. Rev. E.* **81**, 036314–036324 (2010).
67. D. Chatterjee, B. Hetayothin, A. R. Wheeler, D. J. King and R. L. Garrell, *Lab Chip* **6**, 199–206 (2006).
68. H. Lee, K.-S. Yun, S. H. Ko and K. H. Kang, *Biomicrofluidics* **3**, 044113–044125 (2009).
69. P. C. Hiemenz and R. Rajagopalan, *Principles of Colloid and Surface Chemistry*. Marcel Dekker, New York (1997).
70. K. H. Kang, I. S. Kang and C. M. Lee, *Langmuir* **19**, 9334–9342 (2003).
71. K. H. Kang, I. S. Kang and C. M. Lee, *Langmuir* **19**, 5407–5412 (2003).
72. H. Ren, R. B. Fair, M. G. Pollack and E. J. Shaughnessy, *Sensors Actuators B* **87**, 201–206 (2002).
73. M.-Y. Zhou and P. Sheng, *Phys. Rev. Lett.* **64**, 882–885 (1990).
74. T. D. Blake, in: *Wettability*, J. C. Berg (Ed.). Marcel Dekker, New York, pp. 251–309 (1993).
75. T. D. Blake and J. M. Haynes, *J. Colloid Interface Sci.* **30**, 421–423 (1969).
76. J. H. Song, R. Evans, Y.-Y. Lin, B.-N. Hsu and R. B. Fair, *Microfluid. Nanofluid.* **7**, 75–89 (2009).
77. S. W. Walker and B. Shapiro, *J. Microelectromech. Syst.* **15**, 986–1000 (2006).
78. S. W. Walker, B. Shapiro and R. H. Nochetto, *Phys. Fluids* **21**, 102103–102129 (2009).
79. H.-W. Lu, K. Glasner, A. L. Bertozzi and C.-J. Kim, *J. Fluid Mech.* **590**, 411 (2007).
80. E. S. Baird and K. Mohseni, *Nanoscale Microscale Thermophys. Eng.* **11**, 109–120 (2007).
81. A. Ahmadi, H. Najjaran, J. F. Holzman and M. Hoorfar, *J. Micromech. Microeng.* **19**, 065003–065010 (2009).
82. A. Arzpeyma, S. Bhaseen, A. Dolatabadi and P. Wood-Adams, *Colloids Surfaces* **323**, 28–35 (2008).
83. Z. Keshavarz-Motamed, L. Kadem and A. Dolatabadi, *Microfluid. Nanofluid.* **8**, 47–56 (2010).
84. H.-W. Lu, F. Bottausci, J. D. Fowler, A. L. Bertozzi, C. Meinhart and C.-J. Kim, *Lab Chip* **8**, 456–461 (2008).
85. F. Mugele, J.-C. Baret and D. Steinhauser, *Appl. Phys. Lett.* **88**, 204106–204109 (2006).
86. S. H. Ko, H. Lee and K. H. Kang, *Langmuir* **24**, 1094-1101 (2008).
87. K. P. Nichols and H. J. G. E. Gardeniers, *Anal. Chem.* **79**, 8699–8704 (2007).
88. F. Brochard, *Langmuir* **5**, 432–438 (1989).
89. O. V. Voinov, *J. Fluid Dyn. (English Transl.)* **11**, 714–721 (1976).
90. E. V. Dussan, *J. Fluid Mech.* **77**, 665 (1976).

91. C. Huh and L. E. Scriven, *J. Colloid Interface Sci.* **35**, 85–101 (1971).
92. R. G. Cox, *J. Fluid Mech.* **168**, 169–194 (1986).
93. R. Bavière, J. Boutet and Y. Fouillet, *Microfluid. Nanofluid.* **4**, 287–294 (2008).
94. F. Brochard-Wyart and P.-G. de Gennes, *Adv. Colloid Interface Sci.* **39**, 1–11 (1992).
95. P.-G. de Gennes, F. Brochard-Wyart and D. Quéré, *Capillarity and Wetting Phenomena: Drops, Bubbles, Pearls, Waves*. Springer, New York (2004).
96. T. D. Blake, *J. Colloid Interface Sci.* **299**, 1–13 (2006).
97. S. F. Kistler, in: *Wettability*, J. C. Berg (Ed.). Marcel Dekker, New York, pp. 311–429 (1993).
98. G. D. Yarnold and B. J. Mason, *Proc. Phys. Soc. B* **62**, 121–125 (1949).
99. S. Glasstone, K. J. Laidler and H. J. Eyring, *The Theory of Rate Processes*. McGraw-Hill, New York (1941).
100. J. I. Frenkel, *Kinetic Theory of Liquids*. Oxford Univ. Press, Oxford (1946).
101. T. D. Blake, A. Clarke and E. H. Stattersfield, *Langmuir* **16**, 2928–2935 (2000).
102. Q. Yuan and Y.-P. Zhao, *Phys. Rev. Lett.* **104**, 246101–4 (2010).
103. A. M. Cazabat, S. Gerdes, M. P. Valignat and S. Villette, *Interface Science* **5**, 129–139 (1997).
104. J. G. Petrov, J. Ralston, M. Schneemilch and R. A. Hayes, *Langmuir* **19**, 2795–2801 (2003).
105. M. Paneru, C. Priest, R. Sedev and J. Ralston, *J. Am. Chem. Soc.* **132**, 8301–8308 (2010).
106. P. García-Sánchez, A. Ramos and F. Mugele, *Phys. Rev. E* **81**, 012303–012307(R) (2010).
107. S. H. Ko, S. J. Lee and K. H. Kang, *Appl. Phys. Lett.* **94**, 194102–3 (2009).
108. S. K. Chung, Y. Zhao, U.-C. Yi and S.-K. Cho, in: *Proc. Int. Conf. MEMS*, Kobe, Japan, pp. 31–34 (2007).
109. D. J. C. M. 'tMannetje, C. U. Murade, D. van den Ende and F. Mugele, *Appl. Phys. Lett.* **98**, 014102–014105 (2011).
110. R. Malk, Y. Fouillet and L. Davoust, *Sensors Actuators B* **154**, 191–198 (2011).
111. P. Sen and C.-J. Kim, *Langmuir* **25**, 4302–4305 (2009).
112. J. M. Oh, S. H. Ko and K. H. Kang, *Phys. Fluids* **22**, 032002–032012 (2010).
113. F. Li and F. Mugele, *Appl. Phys. Lett.* **92**, 244108–244111 (2008).